

The Phase Space Structure in the vicinity of vertical Lyapunov orbits around $L_{1,2}$ in a barred galaxy model

M. Katsanikas,^{1*} P.A. Patsis,^{1†}

¹Research Center for Astronomy, Academy of Athens, Soranou Efessiou 4, GR-115 27, Athens, Greece

AcceptedReceivedin original form

ABSTRACT

We study the phase space structure and the orbital diffusion from the vicinity of the vertical Lyapunov periodic orbits around the unstable Lagrangian points $L_{1,2}$ in a 3D barred galaxy model. By perturbing the initial conditions of these periodic orbits, we detected the following five types of orbital structures in the 4D spaces of section: (i) Ring-like structures, sticky for large time intervals to the unstable invariant manifolds of the simple and double unstable vertical Lyapunov periodic orbits. (ii) 2D tori belonging to quasi-periodic orbits around stable periodic orbits existing in the region. They are associated either with vertical stable periodic orbits around $L_{4,5}$ or with “stable anomalous” periodic orbits. (iii) Orbits sticky for large time intervals to these tori, forming “sticky tori”, before they slowly depart from them. (iv) Clouds of points that have a strong chaotic behavior. Such clouds of consequents have slow diffusion speeds, because they are hindered by the presence of the tori around the “stable anomalous” periodic orbits. (v) Toroidal zones consisting of points that stick for long time on the unstable invariant manifolds of the “unstable anomalous” periodic orbits. By continuing the integration, we find that eventually they become strongly chaotic, retaining however small diffusion speeds, due to the presence of the tori around the stable anomalous periodic orbits.

Key words: Galaxies: kinematics and dynamics – chaos – diffusion structure

1 INTRODUCTION

In this paper we study the phase space in the vicinity of “vertical” Lyapunov periodic orbits around the unstable Lagrangian points $L_{1,2}$ of a three dimensional (3D) model for barred galaxies.

There are two families of (Lyapunov) periodic orbits (POs) around $L_{1,2}$, namely the planar (pLPO) (see e.g. Romero-Gómez et al. 2009; Tsoutsis et al. 2009; Sánchez-Martin et al. 2016) and the vertical (vLPO) family (Ollé and Pfenniger 1998; Romero-Gómez et al. 2009). The latter orbits are called “vertical”, due to their orientation with respect to the equatorial plane. In effect, there are two vLPO families, one around L_1 and another around L_2 , thus whenever needed to be distinguished, we will call them vLPO1 and vLPO2, respectively. The same occurs for the equilibrium points $L_{4,5}$ and we will call the corresponding vLPO families as vLPO4 and vLPO5, respectively.

We want to examine the phase space close to vLPOs, at the ends of a bar. In order to achieve this goal, we investigate the role of stickiness in three dimensions around equilibrium points, as well as the role of the phase space environment in hindering orbits with initial conditions in the neighborhood of the vLPO’s to diffuse to large chaotic seas. Thus, knowledge of the presence and stability of

other POs in the region is important in our study. Furthermore, we want to study the relationship between diffusion and chaoticity of the orbits, which is a general problem in dynamical astronomy and nonlinear dynamics.

A standard method for studying the structure of phase space is by means of spaces of section. As described in standard textbooks about nonlinear phenomena in Hamiltonian systems (see e.g. Contopoulos 2004, section 2.11.11), a 3D galactic Hamiltonian model has a 6D phase space, which is reduced by the Jacobi constant in time-independent models to a 5D space. By considering a space of section, we establish a well defined 4D symplectic map (Poincaré map) (Poincaré 1892) in a 4D phase space. Eventually, the study of the 6D phase space of a 3D autonomous Hamiltonian system ends up to the study of the 4D phase space of a 4D symplectic map.

The basic problem of the study of the 4D phase space is its visualization. Several methods have been proposed in the past for the visualization of the 4D phase space: 2D and 3D projections (Contopoulos & Barbanis 1989; Vrahatis et al. 1997), stereoscopic projections (Froeschlé 1970; Contopoulos et al. 1982), 2D and 3D slices of 3D subspaces (Froeschlé 1970; Froeschlé 1972; Richter et al. 2014), the method of color and rotation (Patsis & Zachilas 1994; Katsanikas & Patsis 2011) and the method of Lagrangian Descriptors (Agaoglou et al. 2019, 2020a,b). As in many of our previous studies, in our present work we use the method of color and rotation. Briefly, in this method we plot an orbit in a 3D sub-

* mkatsan@academyofathens.gr (MK)

† patsis@academyofathens.gr (PAP)

space of the 4D phase space of the 4D Poincaré map. Then, we use standard graphical packages to rotate the 3D figure and understand its shape. Finally, we color every point of this 3D projection, i.e. each consequent, according to its fourth coordinate. The rotation helps us in order to understand the 3D topology of the structures in the phase space. The color variation indicates if this topology exists in the 4D space or not. This method helps us to distinguish between order and chaos by relating specific 3D structures accompanied by specific patterns of color, to specific cases of orbital stability (see section 3). The method has been used in galactic Dynamics (Katsanikas & Patsis 2011; Katsanikas et al. 2011b,a, 2013; Patsis and Katsanikas 2014a,b), in a 4D symplectic map (Zachilas et al. 2013), in Astrodynamics (Geisel 2013) and in a system of spinning test particle moving in the spacetime background of a Kerr black hole (Lukes-Gerakopoulos et al. 2016).

An important phenomenon that is crucial for the study of the phase space, and plays crucial role in our paper, is the phenomenon of stickiness. There are two kinds of stickiness:

(i) **Stickiness on tori:** In the neighborhood of a stable periodic orbit, the KAM (Kolmogorov-Arnold-Moser) theorem (see Kolmogorov 1954; Arnold 1963; Moser 1962), guarantees the existence of N -dimensional invariant tori in Hamiltonian systems with N degrees of freedom. When the perturbation increases a particular torus is destroyed and it becomes a cantor, a Cantor set of points that is nowhere dense, (see for example Contopoulos 2004, section 2.7). This object has a countable infinity of gaps. When a last KAM torus is destroyed, the small chaotic regions that were inside it are connected with the large chaotic sea that surrounds this last KAM torus. This can happen after a long integration time. This means that the region just inside a cantor is characterized by a large density of points for long time intervals before these points start to diffuse in the large chaotic sea. This is the phenomenon of stickiness and the formed region is called a sticky torus. Stickiness has been extensively studied in Hamiltonian systems of two degrees of freedom (see for example Contopoulos 2004) and in Hamiltonian systems of three degrees of freedom (see for example Katsanikas & Patsis 2011).

(ii) **Stickiness in chaos:** In the neighborhood of unstable periodic orbits, there are two kinds of invariant manifolds, the unstable and stable invariant manifolds (see for example Contopoulos 2004, section 2.5). All orbits with initial conditions on these objects approach the periodic orbit (stable manifold) and move away from the periodic orbit (unstable manifold). In some cases, orbits are stuck for a long time interval in a specific chaotic region of the phase space far away from the invariant tori. This is due to the fact that these orbits are stuck for a long time interval on the unstable invariant manifolds of unstable periodic orbits (see Contopoulos & Harsoula 2013). This is the phenomenon of stickiness in chaos and it has been studied in Hamiltonian systems with two (Contopoulos & Harsoula 2013) and three (Katsanikas et al. 2013) degrees of freedom.

The phenomenon of stickiness refers to chaotic orbits that remain in a specific region of the phase space for a significant time interval. It has to be distinguished from another category of chaotic orbits, that remain in a specific region of the phase space, which is the partially chaotic orbits that obey one isolating integral besides the energy and are bounded by regular orbits (see Muzzio 2017, 2018; Carpintero & Muzzio 2020). Latter, it will not be discussed in the present paper.

In section 2, and in section 3 we briefly present the model which we use and some definitions related to the stability and the

morphology of periodic orbits. In section 4, we study the phase space of our system using the method of 4D spaces of section and we compare our results with Lyapunov Characteristic Numbers. In section 5, we compute the diffusion speed for the different types of phase space objects we encountered in our study. Finally, we discuss our results and we present our conclusions in section 6.

2 THE MODEL

For the purposes of the present paper, we will continue using the Ferrers bar model we have already used in several papers in the past (e.g. Skokos et al. 2002a; Patsis and Katsanikas 2014a; Patsis & Athanassoula 2019; Patsis et al. 2022). It is a popular and extensively studied model for 3D bars, initially used by Pfenniger (1984). The general model consists of a Miyamoto disc, a Plummer bulge and a 3D Ferrers bar. As this part of information is repeated in all the above mentioned papers, we avoid giving it again here and we restrict ourselves in a general description of the model and in giving the values of the parameters we used. For details the reader is referred to the above mentioned papers.

The Miyamoto disc has horizontal and vertical scale lengths, A and B respectively, while its total mass is M_D . The total mass of the spheroidal Plummer bulge is M_S and its scale length is ϵ_s . The numerical values of these parameters are given in in Table 1.

For the axes of the Ferrers bar we set $a : b : c = 6 : 1.5 : 0.6$, as in Pfenniger (1984), while its mass is M_B . The masses of the three components satisfy $G(M_D + M_S + M_B) = 1$, where G is the gravitational constant. The length unit has been taken as 1 kpc, the time unit as 1 Myr and the mass unit as $2 \times 10^{11} M_\odot$. If not otherwise indicated, the lengths mentioned everywhere in the paper are in kpc. Units will be not repeated on the axes of the figures.

The total potential of our model is given in Cartesian coordinates (x, y, z) by

$$\Phi(x, y, z) = \Phi_D + \Phi_S + \Phi_B, \quad (1)$$

where Φ_D, Φ_S and Φ_B are the potentials of the disk, the bulge (spheroid) and the bar respectively.

The 3D bar is rotating around its short z axis counterclockwise, with an angular speed Ω_b . The x axis is the intermediate and the y axis the long one. The equations of motion are derived from the Hamiltonian governing the motion of a test-particle. It can be written in the form:

$$H = \frac{1}{2}(p_x^2 + p_y^2 + p_z^2) + \Phi(x, y, z) - \Omega_b(xp_y - yp_x), \quad (2)$$

where p_x, p_y , and p_z are the canonically conjugate momenta. We will hereafter denote the numerical value of the Hamiltonian by E_j and refer to it as the Jacobi constant or, more loosely, as the ‘energy’.

The parameters referring to the masses of the three components, the pattern speed, the E_j ’s of the important for our study resonances and the corotation distance, can also be found in Table 1.

3 PERIODIC ORBITS AND THEIR STABILITY

The space of section of 3D systems is 4D. In order to study the vertical periodic orbits around the Lagrangian points $L_{1,2}$ we use the space of section $z=0, p_z > 0$ and we integrate the equations of motion for a given value of the Hamiltonian. Our initial conditions are $(x_0, p_{x_0}, y_0, p_{y_0})$. We find the initial conditions for a PO by using a

Table 1. The parameters used in our model: G is the gravitational constant, M_D , M_B , M_S are the masses of the disc, the bar and the bulge respectively, A and B the horizontal and vertical scale lengths of the Miyamoto disc respectively, ϵ_s is the scale length of the spheroidal bulge, Ω_b is the pattern speed of the bar, $E_j(L_{1,2})$, $E_j(L_{4,5})$ are the values of energy of the equilibrium points $L_{1,2}$ and $L_{4,5}$ and R_c is the corotation radius

GM_D	GM_B	GM_S	A	B	ϵ_s	Ω_b	$E_j(L_{1,2})$	$E_j(L_{4,5})$	R_c
0.72	0.2	0.08	3	1	0.4	0.054	-0.2029	-0.1976	6.31

Table 2. The initial conditions of the periodic orbits of the families $vLPO1, 2$, $vLPO4, 5$, z -axis family, sao and uao in the Poincaré section $z = 0$ with $p_z > 0$ for $E_j = -0.165$.

Family	x	y	p_x	p_y
$vLPO1$	0	6.03566990	-0.2549905669	0
$vLPO2$	0	-6.03566990	0.2549905669	0
z -axis family	0	0	0	0
$vLPO4$	5.7038012135	0	0	0.2551977174
$vLPO5$	-5.7038012135	0	0	-0.2551977174
sao and its symmetric	2.1463697858	0	0	-0.2468369233
	-2.1463697858	0	0	0.2468369233
uao and its symmetric	0	2.1265112564	0.4100251830	0
	0	-2.1265112564	-0.4100251830	0

Newton iterative method. We consider a PO as been located, when the initial and final coordinates coincide with an accuracy of at least 10^{-11} . We used a fourth order Runge-Kutta scheme for the numerical integration of the periodic orbits, keeping the relative error in the energy smaller than 10^{-15} .

In order to compute the stability of a PO we follow the method of Broucke (1969). For this, we first consider small deviations from its initial conditions in the space of section $z=0$, $p_z > 0$ and we integrate this ‘‘perturbed’’ orbit to the next upward intersection with the space of section. In this way a 4D map $T : \mathbb{R}^4 \rightarrow \mathbb{R}^4$ is established, which relates the initial with the final point. The relation of the final deviations of this, neighboring to the periodic orbit, to the initially introduced deviations, can be written in vector form as: $\vec{\xi} = M \vec{\xi}_0$. Here $\vec{\xi}$ is the final deviation, $\vec{\xi}_0$ is the initial deviation and M is a 4×4 matrix, called the monodromy matrix. The eigenvalues of the monodromy matrix can determine the kind of linear stability of a periodic orbit. If a periodic orbit has two pairs of eigenvalues on the unit circle, it is stable. Otherwise, the periodic orbit is unstable. There are three kinds of instability for periodic orbits: simple instability, double instability, and complex instability. Simple and double instability are the cases where the periodic orbits have one pair of eigenvalues on the unit circle and one on the real axis (simple instability) or two pairs on the real axis (double instability), as described in Contopoulos & Magnenat (1985). Finally, complex instability (see eg. Contopoulos & Magnenat 1985; Pfenninger 1985a,b; Zachilas 1993; Patsis & Zachilas 1990; Stöber & Bäcker 2021; Patsis et al. 2022; Jorba & Olle 2004) is the case in which the eigenvalues of the periodic orbits form a complex quadruplet that is off the unit circle.

In order to have an overall impression for the dynamical behaviour of the two $vLPO$ families, which have as origin either of the Lagrangian points $L_{1,2}$, we computed their orbits and we followed the evolution of their stability by means of the Broucke method. These orbits have on the 4D space of section initial conditions $(x_0, p_{x_0}, y_0, p_{y_0})$ with $(0, y > 0, p_x < 0, 0)$ and $(0, y < 0, p_x > 0, 0)$

respectively. Following the evolution of their b_1 and b_2 indices (Contopoulos & Magnenat 1985), we found that they are in general simple unstable, with a rather small double unstable energy interval for $-0.1876 < E_j < -0.1707$, which is located beyond $E_j(L_{4,5})$.

The morphology of the members of the $vLPO$ family have a ‘‘bent-eight’’ morphology (red orbits in Fig. 1), similar to the morphology of the vertical families around the stable Lagrangian points $L_{4,5}$ (green orbits in Fig. 1). This is in agreement with the findings of Ollé and Pfenninger (1998) and Romero-Gómez et al. (2009). The depicted in Fig. 1 $vLPO$ ’s, at $E_j = -0.165$, reach heights $|z| \approx 3.7$ away from the equatorial plane. In Fig. 1 we give also the representatives of two families introduced by Heisler et al. (1982), namely of the stable and unstable anomalous orbits (sao and uao respectively). The role of these families will be examined in section 4.5. The positions of the periodic orbits of these families in the Poincaré section $z = 0$ with $p_z > 0$ (for value of energy $E_j = -0.165$) are given in table 2.

4 THE PHASE SPACE

We apply the method of color and rotation, in order to visualize the phase space structure in the vicinity of $vLPO$ s around $L_{1,2}$. For this reason, we choose to study the phase space structure in the vicinity of $vLPO$ s $L_{1,2}$ for a value of energy $E_j = -0.165$, which is larger than the energy of the equilibrium points $L_{1,2}$. We do so, because we want to study not only the phase space geometry close to $vLPO1$ and $vLPO2$ but all the possible phase space objects that are emanated from the equilibrium points L_3 and $L_{4,5}$ and could affect the phase space structure close to $vLPO$ s around $L_{1,2}$. Thus, we need a value of energy at which representatives of all involved families of periodic orbits exist.

In our 4D space of section $z=0$, with $p_z > 0$ we input the four initial conditions (x, y, p_x, p_y) and we plot each orbit in a 3D subspace of the 4D space of section, e.g. in the subspace (x, y, p_x)

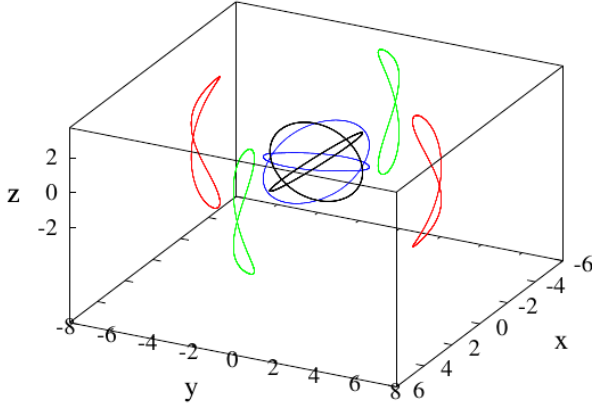


Figure 1. The pair of vLPOs around $L_{1,2}$ and the two periodic orbits of the vertical families around $L_{4,5}$ are given with red and green color respectively, at $E_j = -0.165$. The two members of sao and its symmetric family, as well as the two members of uao and its symmetric family are plotted with black and blue color respectively, for the same energy.

and we color the consequents according to their fourth coordinate, i.e. according to their p_y values.

The phase space objects we encountered belong to two categories. The phase space objects of the first category are obtained if we perturb the initial conditions of the vLPO1,2. These objects are:

(i) **Ring like structures** that are described in subsection 4.1. A kind of these phase space objects are reached by applying a perturbation to all four initial conditions in the ranges: $-5 \leq \Delta x \leq 5.2$, $-3.9 \leq \Delta y \leq 4$, $-0.02 \leq \Delta p_x \leq 0.09$ and $-0.2 \leq \Delta p_y \leq 0.2$. These phase space objects are due to the phenomenon of stickiness in chaos (see the subsection 4.4).

(ii) **Clouds** result for larger perturbations as described in subsection 4.2.

The phase space objects of the second category are obtained if we perturb the initial conditions of the vLPO4,5. They are tori and sticky tori (see subsection 4.3). Finally, the role of the z-axis family and its bifurcations to the structure of the phase space is analyzed in section 4.5.

4.1 Ring like structures, aka double crescents

The first type of structure we encounter in the neighborhood of vLPOs around $L_{1,2}$ in phase space, is a ring-like one, resembling a double crescent, with the two crescents facing and touching each other at their horns. Hereafter, we will briefly refer to this shape as the “double-crescent”. The fourth dimension in this case follows the topology of this structure in the 3D subspace of the phase space as the color-rotation method reveals. An example is given in Fig. 2. In order to obtain the depicted orbit, we have considered the simple unstable vLPO at $E_j = -0.165$ and we applied a perturbation $\Delta y = 10^{-4}$ in its initial conditions. However, we obtain similar double-crescent structures, by applying perturbation: $-5 \leq \Delta x \leq 5.2$, $-3.9 \leq \Delta y \leq 4$, $-0.02 \leq \Delta p_x \leq 0.09$ and $-0.2 \leq \Delta p_y \leq 0.2$. For initial conditions outside these ranges we may find clouds of points or we cross the surface of zero velocity and then we are beyond the phase space region in which we are allowed to integrate our orbits. (We remind that $E_j = -0.165 > E_j(L_{4,5}) > E_j(L_{1,2})$).

The structure depicted in Fig. 2 consists of the first 190 con-

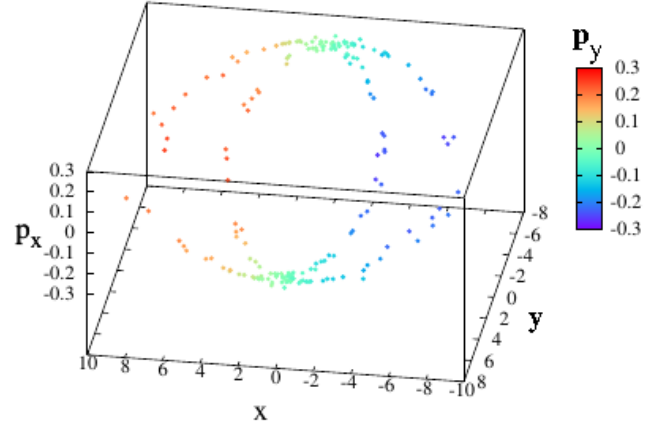


Figure 2. The 3D representation (x, y, p_x) of the double-crescent structure for the first 190 intersections with the space of section $z = 0$ with $p_z > 0$. Every point is colored according to the fourth dimension p_y (color bar at the right-hand side of the figure).

sequents of the orbit in the 4D space of section. These 190 consequents, correspond already to $t = 13$ Gyrs. For finding the chaoticity of these orbits we have to extend our calculations to unrealistic large time intervals. However, this allows us to understand the underlying dynamical mechanism and also helps us estimating the expected orbital dynamics in specific volumes of the phase space. It can be considered as confined within a narrow cylinder with dimensions about $[-10, 10] \times [-8, 8]$ in the (x, y) plane and a much smaller thickness of about 0.6 in the third dimension p_x . The p_y “colours”, evidently, follow a smooth color variation (cf. with the color bar at the right-hand side of the figure) which reflects the fact that the consequents are on, or at least close to, a smooth surface in the 4D space. However, if we continue integrating the orbit, the consequents start diffusing in the surrounding phase space and we observe a mixing of colors. For other double crescent orbits, with initial conditions in the previously indicated ranges, this happens even earlier, when the orbits have formed only part of the double-crescent structure. At any rate, this evolution clearly indicates stickiness, or a weakly chaotic behaviour.

When diffusion starts, the consequents form eventually a cloud where colors are mixed. The scattering of points in the 3D subspace and the mixing of colors indicate the strong chaotic behavior and the transition from the state of stickiness to the state of strong chaoticity. Furthermore, we observe that the diffusion of points leads to the occupation of a larger volume in phase space. As we see in Fig. 3, already for 382 intersections of the orbit with the space of section the occupied volume is $[x_1, x_2] \times [y_1, y_2] \times [p_{x1}, p_{x2}] \times [p_{y1}, p_{y2}] = [-20, 25] \times [-30, 40] \times [-0.4, 0.4] \times [-0.4, 0.4]$. This is a larger volume than the one of the narrow cylinder within which the first 190 consequents are confined. We also observe that the 382 consequents drift away from the vLPOs mainly on the (x, y) plane, while their $|p_y|$ values increase their extent by 33% with respect to the values during the first 190 intersections. Eventually the points form clouds like these that are described in the next subsection.

The orbit in Fig. 2 and Fig. 3, integrated over one Hubble time in the (x, y, z) space is given in Fig. 4. The (x, y) projection retains a double-crescent morphology similar to the one we have found existing in the (x, y, p_x) space in Fig. 2. Nevertheless, we have to keep in mind that in Fig. 2 we depict a space of section, while in Fig. 4 we plot the orbit in the configuration space. It is remarkable that

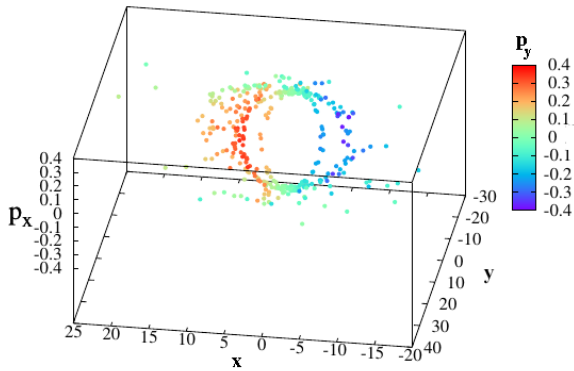


Figure 3. The 3D representation (x, y, p_x) of the double-crescent structure for 382 intersections with the space of section $z = 0$ with $p_z > 0$. Every point is colored according to the fourth dimension p_y .

this overall morphology is one frequently observed in barred galaxies such as NGC 1326 and NGC 3504 Sandage & Bedke (1994), or NGC 2665 (Red DSS image as in NED/NASA). Although this structure is expected to be supported by planar orbits (see e.g. figure 21 in Kaufmann & Contopoulos 1996), we see that the projection of sticky orbits reaching high z retains this morphology.

As we can observe in the left panel of Fig. 4, the orbit spends more time in the neighborhood of L_1 and L_2 , which results in the formation of two dense regions around the two unstable equilibrium points in the face-on, (x, y) , view. In the end-on, (x, z) projection, these two dense regions correspond to the central, dense part, filling roughly a $(-4, 4) \times (-4, 4)$ region, while the orbit extends in the x -direction close to a distance from the center of about 8. Finally, in the side-on, (y, z) , projection, these two dense regions coincide with the two parenthesis-like arcs at the sides of this projection of the orbit (Fig. 4 right panel).

In order to estimate the chaoticity of the orbit, we used the standard “finite time” Lyapunov Characteristic Number indicator (see e.g. Contopoulos 2004, section 2.10 and references therein). For this we computed the quantity $LCN(t) = \frac{1}{t} \ln \left| \frac{\xi(t)}{\xi(t_0)} \right|$, in which $\xi(t_0)$ and $\xi(t)$ are the distances between two points of two nearby orbits at times $t = 0$ and t respectively. The evolution of $LCN(t)$ with time is given in Fig. 5. We observe that it has some fluctuations until the time at which the consequents leave the double-crescent structure (indicated with an arrow). Thereinafter, it increases slowly but constantly, tending to a positive value equal to 4.6×10^{-3} . This evolution confirms the sticky-chaotic character of the orbit.

4.2 Clouds

As we mentioned earlier, by increasing the absolute value of the perturbations, we reach initial conditions of orbits in the neighborhood of vLPOs, which rapidly demonstrate a chaotic character. Such orbits are represented in the 4D space of section by clouds of consequents with an irregular distribution in the 3D subspaces. They also have an irregular distribution in the fourth dimension, reflected in the mixing of their colors. An example with a $\Delta y = -4$ perturbation, always for $E_j = -0.165$ is given in Fig. 6. This picture points to a strong chaotic behavior. The evolution of $LCN(t)$, given in Fig. 7, confirms this conclusion, since, after some initial fluctuations, it tends to a relatively large positive number, i.e. to 10^{-2} .

The projections of this orbit in the configuration space can be described as roundish, with irregular shapes, as we can observe in Fig. 8. The orbit is integrated again for a Hubble time, which corresponds now to 343 intersections with the $z = 0$ plane. These initial conditions lead to an irregular morphology of an orbit. Nevertheless, the orbit during the integration period, remains inside corotation. This is a counter-intuitive result, since the energy of the orbit is larger than the energy of the Lagrangian points at corotation, starting however well inside the corotation radius $R_c = R_{L_1} = 6.31$.

Despite the fact that the clouds of points indicate a strong chaotic behavior, their consequents remain confined in the 4D space of section within a region $[-8, 8] \times [-6, 6] \times [-1, 1] \times [-1, 1]$, which corresponds to a smaller volume than the region occupied by the 190 consequents of the sticky, double-crescent orbit in Fig. 2. The origin and the conditions for this weak diffusion will be investigated below.

4.3 Tori and sticky tori

According to the KAM theorem (Kolmogorov 1954; Arnold 1963; Moser 1962) in a near-integrable, 3D system, such as the one we study here, there are orbits that lie on 3D invariant tori close to stable POs. These invariant tori are 2D objects in the 4D space of section. Such objects are the invariant tori around the periodic orbits vLPO4,5. The POs of these families are stable and have initial conditions $(x > 0, 0, 0, p_y > 0)$ (for L_4) and $(x < 0, 0, 0, p_y < 0)$ (for L_5). An example of these tori is given in Fig. 9, depicting the perturbed by $\Delta x = 0.6$ vertical PO around L_4 . This torus has in the 4D space of section the morphology of a rotational torus (Vrahatis et al. 1997; Vrahatis et al. 1996). This kind of tori have a smooth color variation on their surfaces, if we colour the consequents of the orbit according to their values in the fourth dimension (Katsanikas & Patsis 2011).

By increasing further the perturbation of the initial conditions of the vLPO4 along the x -direction, we encounter a different dynamical behaviour for $\Delta x = 1.3$. In this case we initially find again a rotational-torus-like structure considering the first 17120 consequents, but for larger integration times the consequents start occupying a larger volume around the periodic orbit (Fig. 10). This is the phenomenon of stickiness on tori (see introduction), as encountered in the case of the tori around stable POs in 3D autonomous Hamiltonian systems. During the sticky period of an orbit it forms a torus-like orbit, which was called sticky torus in Katsanikas & Patsis (2011). Such tori are unstable and present a weak chaotic behavior. For usual time scales in Galactic Dynamics, the dynamical behavior of such orbits can be considered practically identical to that of regular orbits.

This weak chaotic behavior can be also identified by means of the finite time $LCN(t)$. However, we need an even larger integration time, than the integration time used when applying the method of color and rotation, in order to appreciate it. In Fig. 11, we observe that the $LCN(t)$, which corresponds to the invariant torus of the Fig. 9 (black curve) tends to zero. During the same time interval, the $LCN(t)$ that corresponds to the sticky torus of Fig. 10 (red curve), initially decreases, behaving like the $LCN(t)$ of an ordered orbit. However, at $t=315000$, it starts increasing and finally it tends to a relatively small positive number 10^{-4} . The $LCN(t)$ identifies the weak chaotic behavior of the sticky torus after 325000 time units, thus this index traces the chaotic behaviour slower than the method of color and rotation.

The difference between this kind of sticky behaviour and the

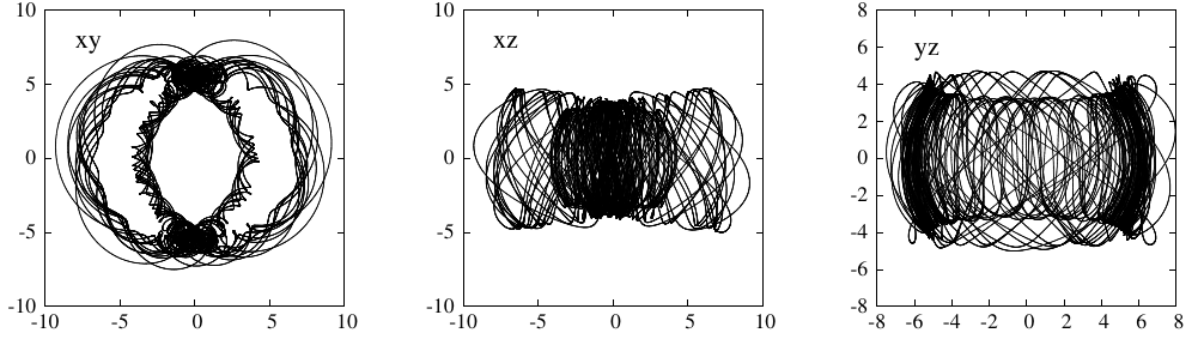


Figure 4. The (x, y) , (x, z) and (y, z) projections of the ring- or double-crescent-like orbit with initial conditions close to L_1 with $E_j = -0.165$, integrated for one Hubble time.

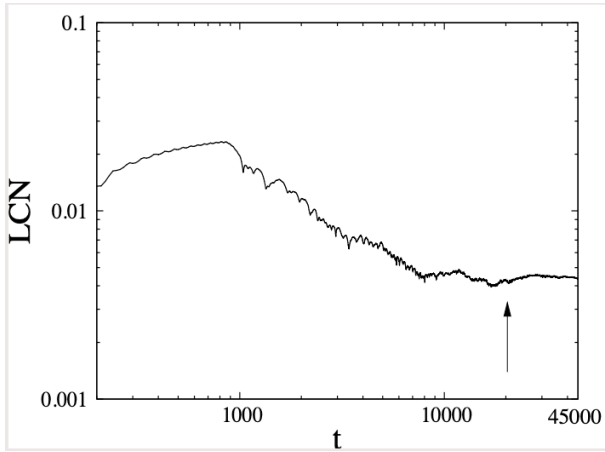


Figure 5. The variation of $LCN(t)$ (in log-scale) for the double-crescent structure. The arrow indicates the time at which the consequents leave the double-crescent structure.

one of the orbit described in section 4.1 is explained in the following paragraph.

4.4 Manifolds around vLPOs and stickiness in chaos

An illustrative way for understanding the structures we encounter in phase space, due to the presence of the vertical families in the neighborhood of L_1 and L_2 for $E_j = -0.165$, is offered by the (x, y) projection of the 4D phase space (x, y, p_x, p_y) . This is presented in Fig. 12. The initial conditions of the vLPOs around L_1 and L_2 are marked with two black squares at $y > 0$ and $y < 0$ respectively. Besides the vertical families around $L_{1,2}$ we have also the vertical families around the stable equilibrium points $L_{4,5}$. In Fig. 12 their locations are indicated with two black “*” symbols.

In Fig. 12, apart from the location of the POs and the projections of the tori, we also plot the projections on the (x, y) plane of the asymptotic curves of the unstable invariant manifolds of the two simple unstable vLPOs around $L_{1,2}$. We plot with green the vLPO around L_1 and with cyan the vLPO around L_2 . The numerical construction of the asymptotic curves is described in detailed in Katsanikas et al. (2013). The unstable invariant manifolds of the simple unstable periodic orbits are 1-dimensional objects in the 4D space of section, because they correspond to one eigenvalue, which is outside the unit circle (Arnold 1988, section 34A). Due to the

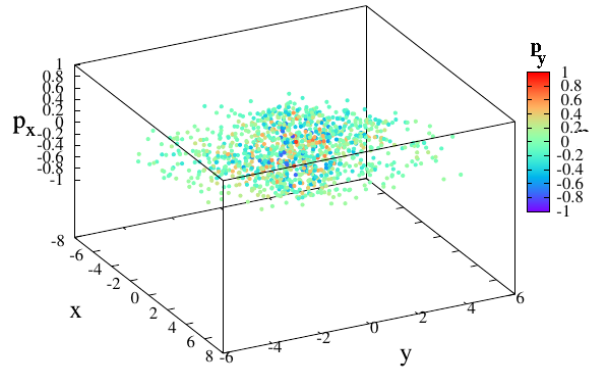


Figure 6. The cloud of points in the 4D space of section $z = 0$ with $p_z > 0$. The consequents of the cloud are plotted in the 3D subspace (x, y, p_x) and it is colored according to the fourth dimension p_y . In the cloud, we observe mixing of colours.

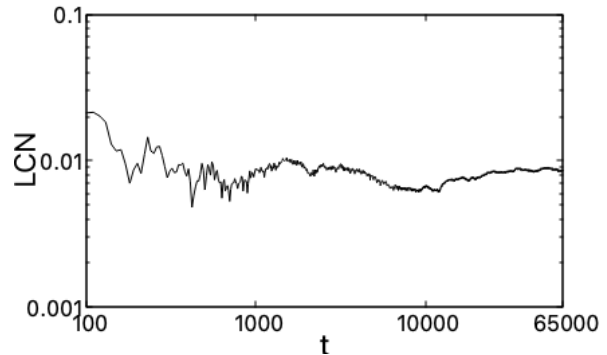


Figure 7. The variation of $LCN(t)$ for the orbit in Fig. 6 (in log-scale).

presence of higher-dimensional objects, namely due to the (blue) invariant tori around the stable vLPO4 and vLPO5, the asymptotic curves are wrapped around them in the 2D projection of the space of section (a similar case has been encountered in Katsanikas et al. 2013). By rotating the figure in 3D subspaces, e.g. in (x, y, p_x) , we realize that the manifolds warp around, without intersecting, the blue tori at a given E_j . The first 190 points of the double-crescent structure (red dots in Fig. 12), stick on the asymptotic curves of the

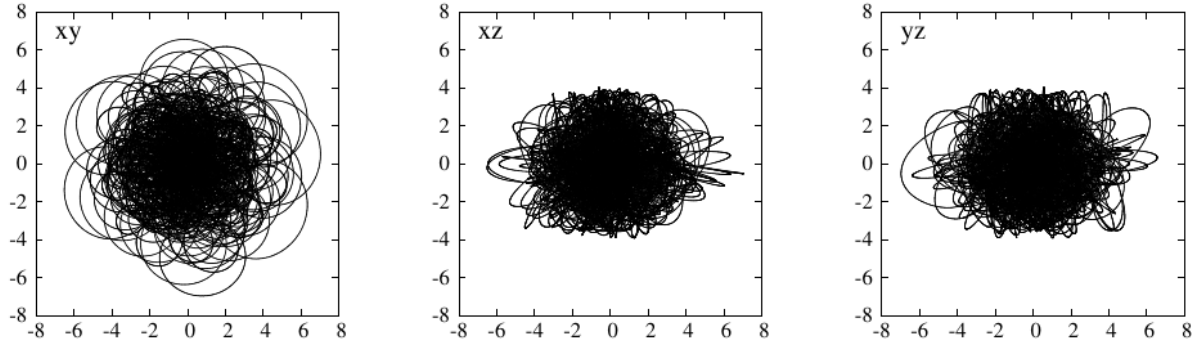


Figure 8. The (x, y) , (x, z) and (y, z) projections of a “cloud orbit” in the configuration space (for one Hubble time).

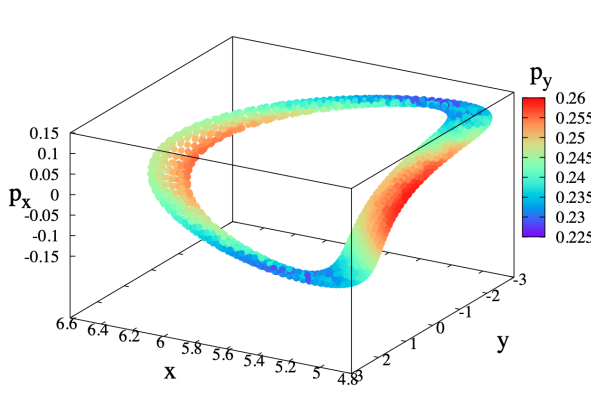


Figure 9. An invariant torus around the Lagrangian point L_4 in the 3D subspace (x, y, p_x) of the 4D space of section $z = 0$ with $p_z > 0$, colored according to the p_y values of the consequents.

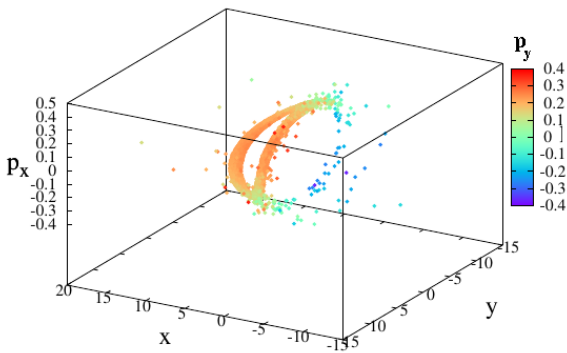


Figure 10. A sticky torus around the Lagrangian point L_4 in the 3D subspace (x, y, p_x) of the 4D space of section $z = 0$ with $p_z > 0$. The color represents the fourth dimension p_y . The consequents depart from the sticky torus after 17120 intersections.

invariant manifolds in the 3D, and consequently on the 2D, projections of the 4D space of section. As we can see in Fig. 2, these 190 consequents have also a smooth color variation, reflecting a smooth distribution of their fourth coordinate (p_y). This sticky-on-manifolds behaviour of the 190 consequents, shows once again, as in Katsanikas et al. (2013), the presence of the phenomenon of stickiness in chaos in galactic type Hamiltonian systems.

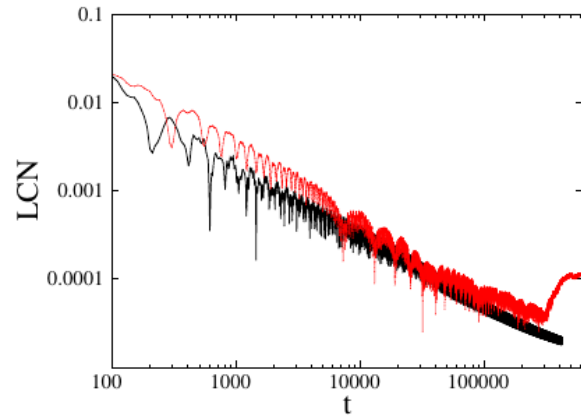


Figure 11. The variation of $LCN(t)$ (with black color) for the case of the invariant torus which is depicted at the Fig. 9. The variation of $LCN(t)$ (with red color) for the case of the sticky torus which is depicted at the Fig. 10. Both axes are in log-scale.

4.5 The role of z-axis and its bifurcations

Finally, for completing our study, we investigate the important for our study “z-axis” orbits and its bifurcations. The POs of the z-axis family lie entirely along the rotating z-axis, i.e. and can be considered as the vertical Lyapunov family of the Lagrangian point L_3 . They have initial conditions $(x, y, p_x, p_y) = (0, 0, 0, 0)$ in the 4D space of section. Heisler et al. (1982) computed this family as well as its two bifurcations, which they named stable and unstable anomalous orbits (sao and uao respectively). Both of these families have at each energy two symmetric representatives. Specifically, the two sao orbits have initial conditions $(x > 0, 0, 0, p_y < 0)$ and $(x < 0, 0, 0, p_y > 0)$ and the two uao $(0, y > 0, p_x > 0, 0)$ and $(0, y < 0, p_x < 0, 0)$. The dynamics and the stability of these families have been later studied by Martinet and Pfenniger (1987) and by Patsis & Zachilas (1990).

The z-axis family is for large regions of the parameter space unstable and in fact complex unstable (Martinet and Pfenniger 1987; Patsis & Zachilas 1990). This is the case also for its representative at $E_j = -0.165$. We find that even a tiny perturbation of its initial conditions leads to chaotic orbits such as the one in Fig. 6. Here we underline the fact that the cloud in Fig. 6 can be obtained by applying a perturbation $\Delta y = -4$ at the initial condition of vLPO1 or applying a $\Delta y = 2.035$ perturbation at the initial condition of the z-axis family. The z-axis orbits, perturbed along the

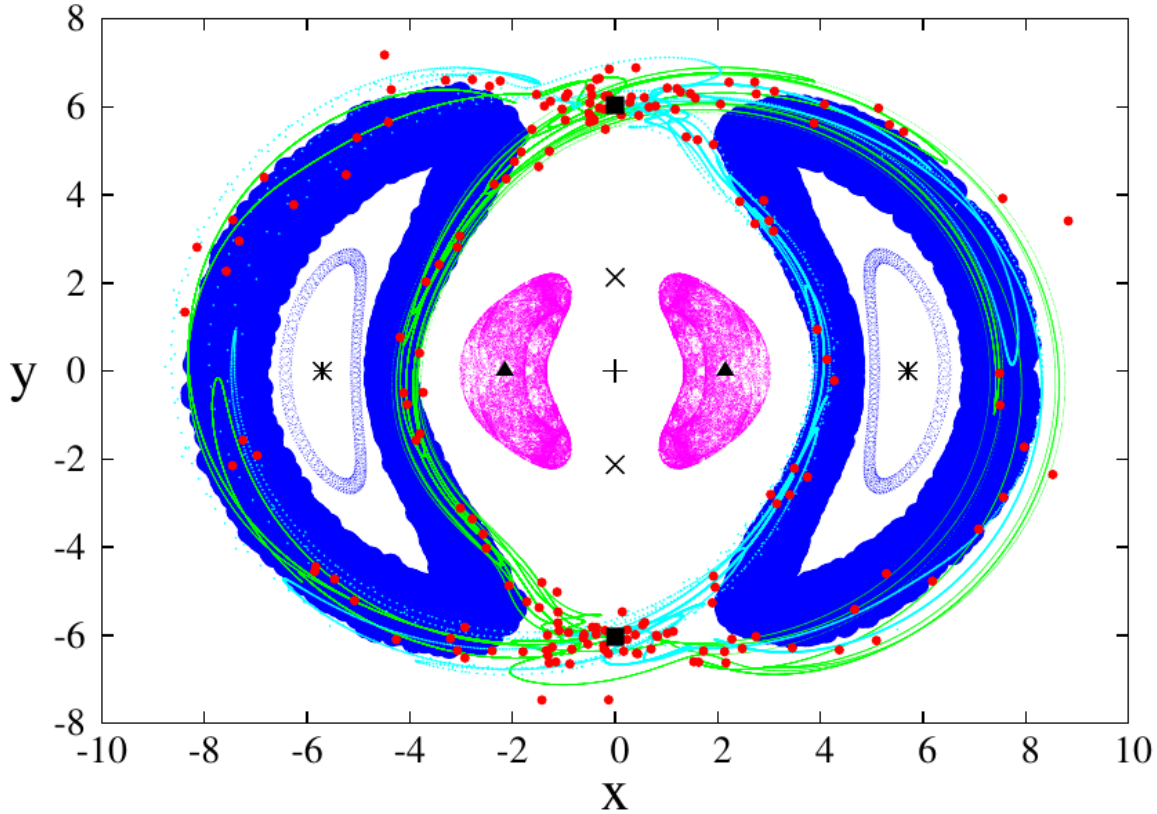


Figure 12. The (x, y) projection of the (x, y, p_x, p_y) 4D space of section, for consequents and invariant manifolds associated with the diffusion of 3D orbits form the neighborhood of vLPOs around L_1 and L_2 for $E_J = -0.165$. We consider $z = 0$ with $p_z > 0$. The initial conditions of the two vLPOs are indicated with black squares, while those of the vertical POs around $L_{4,5}$ with black stars. Furthermore, the central cross corresponds to the initial conditions of the POs of the z -axis family (coincides with the location of L_3), black triangles mark the location of the two sao POs and the \times symbols those of the two uao ones. The 190 consequents of the double-crescent orbit are given with heavy red dots. The 2D projection of the unstable invariant manifolds of the simple unstable vLPOs around L_1 and L_2 are drawn with green and cyan color respectively. The projections of the tori around the stable $L_{4,5}$ are drawn with blue, while those around the sao POs with magenta color. This landscape offers an illustrative representation of the main structures existing in the phase space we study.

y -direction, keeping the rest of the initial conditions equal to zero, demonstrate this behavior for $|y_0| < 2.5$. However, these chaotic orbits do not easily cross the $L_{1,2}$ regions to visit the zone of the model beyond corotation. The origin of this behaviour becomes apparent by inspection of Fig. 13, where we present an orbit perturbed by $\Delta y = 10^{-3}$. We remind that we observe the same behaviour also for larger perturbations. For example we obtain the same orbit depicted in Fig. 6, also by applying a $\Delta y = 2.035$ to the initial conditions of the z -axis orbit. The existence of the magenta invariant tori around the two sao orbits, assisted by the presence of the blue invariant tori around the vertical POs around $L_{4,5}$ hinder the diffusion of the chaotic orbits and keep them trapped in the central region of the (x, y, p_x) projection. The few consequents that overcome the two tori barriers stick on the blue tori that are around the v $L_{4,5}$ (Fig. 13).

Perturbations of the bifurcations of the z -axis (sao and uao) lead to different structures in phase space, as expected, since the sao orbits are stable while those of the uao families are unstable. Perturbations of sao lead to quasi periodic orbits, the tori of which have been presented in Fig. 12. On the other hand, by adding even tiny perturbations, like $\Delta x = 10^{-3}$, in the initial conditions of the uao POs, we find in the 3D (x, y, p_x) subspace ring-like objects. Such an orbit, with the aforementioned perturbation at $E_J = -0.165$, is given in Fig. 14 and we will refer to it as a ‘‘toroidal structure’’.

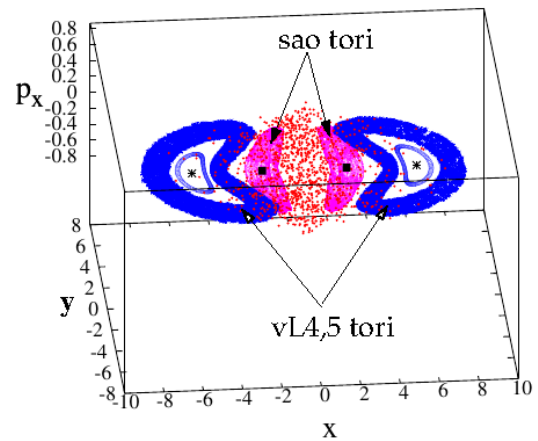


Figure 13. The 3D (x, y, p_x) projection of the cloud (red dots) in the 4D space of section $z = 0$ with $p_z > 0$ for $\Delta y = 10^{-3}$, always for $E_J = -0.165$. The 3D projection of the invariant tori around the vertical POs around $L_{4,5}$ and the 3D projection of the invariant tori around the POs of the two sao families are represented by blue and magenta color respectively.

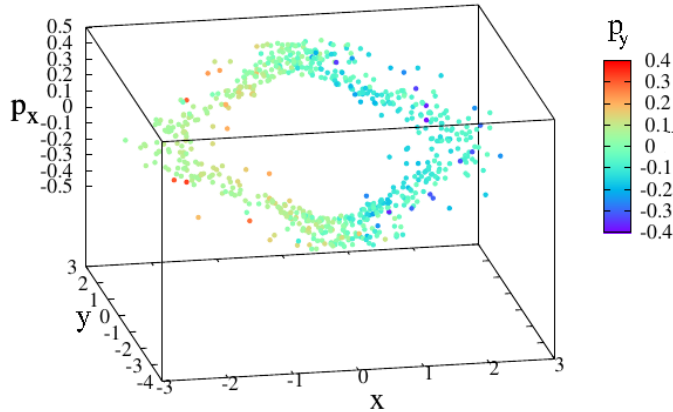


Figure 14. A 4D representation of the space of section for the first 700 consequents of the toroidal zone. The spatial coordinates are (x, y, p_x) , while the colour of the consequents represents their p_y value.

Despite the fact that, vaguely speaking, it has a toroidal topology, its actual shape is irregular. The consequents do not lie on a smooth surface in this 3D projection. We observe that the consequents building this structure have a rather smooth color variation, albeit some points already are departing from it at the end of the integration time. All these point to a weakly chaotic orbit. Its morphology in the configuration space, integrated over a Hubble time, is given in Fig. 15. It remains confined in a (x, y, z) region $[-3, 3] \times [-3, 3] \times [-3, 3]$, with a toroidal face-on and a spheroidal edge-on view.

We computed the unstable invariant manifolds of the simple unstable uao POs, as well as of its symmetric family, and we present them for $E_j = -0.165$ in Fig. 16, with green and cyan color respectively. For the computation we followed again the steps described in detail in Katsanikas et al. (2013). Also in this case the unstable asymptotic curves of a simple unstable PO are guided from the invariant tori that exist in the region. In the present case, they are guided by the invariant tori around the two sao orbits, drawn with magenta color in Fig. 16.

The first 700 consequents of the toroidal structure depicted in Fig. 14 stick on the unstable invariant manifolds of the two uao POs (Fig. 16). We observe again the presence of stickiness in chaos, as in the case of the double-crescent structure (Fig. 12). However, as expected for a sticky orbit, by continuing the integration, we have a transition from the toroidal-like structure depicted in Fig. 14, to a cloud of points, with mixing of colors in the fourth dimension and a strongly chaotic behaviour of the orbit.

This transition is reflected also in the variation of its $LCN(t)$. In Fig. 17 we observe a behaviour of this chaos indicator similar to that of the orbit in Fig. 5. Beyond the point indicated with an arrow, it levels off at a positive number of the order of 10^{-2} . Nevertheless, again due to the presence of the magenta tori in Fig. 16, the consequents of the toroidal structure remain confined for a long time in a restricted zone of phase space and this is also compatible with the morphology of the orbit in the configuration space (Fig. 15).

5 DIFFUSION

We come now to the study of the diffusion of chaotic orbits located in the neighborhood of the vLPOs around $L_{1,2}$. The four types of chaotic orbits we discussed in Section 4 are the double-crescent

structures, the clouds of points, the sticky tori (that are around vLPO_{4,5} and sao orbits) and the toroidal structures close to the periodic orbits of uao and its symmetric one. For these types of orbits we computed their diffusion speed as defined in Katsanikas et al. (2013). The estimation of the diffusion is based on the estimation of V_d , the diffusion volume. For this we compute, as time increases, the volume of the hypersphere on the 4D space of section, with center the position of the periodic orbit and radius the mean distance of the consequents from the periodic orbit. The diagram of V_d versus t gives us valuable information about the diffusion of the orbits. We call T_d (diffusion time) the time needed by an orbit to reach the maximum V_d (V_{max}), while the ratio V_{max}/T_d gives us what we call “diffusion speed”, u_d (Katsanikas et al. 2013). We underline the fact that the most important information is obtained through the diagram V_d versus t (the information given by V_{max} and by the diffusion speed is complementary). This diagram can distinguish different kinds of orbital behavior (regular, weakly chaotic, and strong chaotic) giving in parallel the time evolution of the diffusion (see Katsanikas et al. 2013). The maximum diffusion volume and the diffusion speed give us only an indication of the maximum diffusion of the orbits and they have a complementary role.

Based on the above definitions, we first compute the diffusion speed of the orbit building the double-crescent structure (Fig. 2). In Fig. 18a we give the variation of V_d with time. At the very beginning of the integration, the diffusion volume increases almost monotonically, then it continues increasing fluctuating tending to a value $V_d \approx 13000$, up to the point indicated with an arrow. Until that time, the orbit remains sticky to the unstable invariant manifolds of the vLPOs around $L_{1,2}$, which are guided by the invariant tori around $L_{4,5}$. For

larger time, the consequents depart from the double-crescent structure (corresponding to 190 intersections with the space of section). We observe a characteristic step in the variation of V_d at this point (Fig. 18a). From this point on, the diffusion volume increases further, tending to a value $V_{max} \approx 28100$, which is reached for $T_d = 45000$. Thus, the diffusion speed of the double-crescent structure is 0.624. The consequents will occupy larger volumes in the phase space as time increases because the system is open (the value of energy is above the value of energy $E(L_{1,2})$ and the consequents cannot be restricted from the curve zero velocity surface). This results the increasing of diffusion volume versus time.

The time evolution of the diffusion volume of the sticky-torus-orbit around L_4 (Fig. 10) is given in Fig. 18b. The diffusion volume is constant for a large time interval ($10000 < t < 45000$). Once the consequents depart from the torus region, at the time indicated with an arrow at the right-hand side of Fig. 18b, we observe a small increase of V_d . This small increase will continue forever because the system is open (the value of energy is above the value of the $E(L_{1,2})$ energy and the consequents cannot be restricted from the curve zero velocity surface). We compute the diffusion speed for this orbit to be $u_d = 0.001034$ ($V_{max} = 1765$ and $T_d = 1707000$).

The orbit that gives the clouds in the space of section (Fig. 6) is strongly chaotic, but, as long as we integrated it, it remains trapped in a subvolume of the phase space, due to the presence of the invariant tori of the sao’s. In this case, the evolution of the diffusion volume is given in Fig. 18c. The values of the volume level off at about $V_d = 8000$, but close to the end of the integration, beyond a time indicated with an arrow, there is a small further increase. This increase is due to the few points that slip through the “holes” between the tori, reaching larger distances. The consequents occupy a maximum diffusion volume $V_d = 9200$ at $T_d = 62000$, which gives a diffusion speed $u_d = 0.14832$.

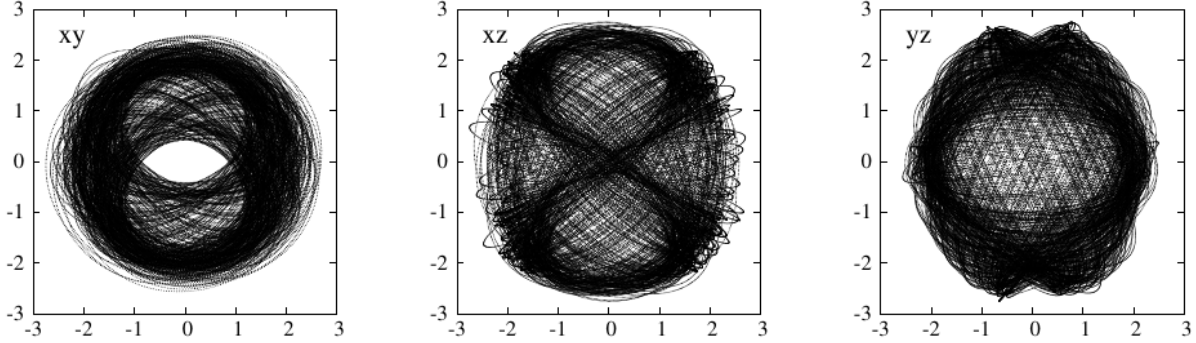


Figure 15. The (x, y) , (x, z) and (y, z) projections of the orbit corresponding to the “toroidal zone” of Fig. 14. integrated for one Hubble time.

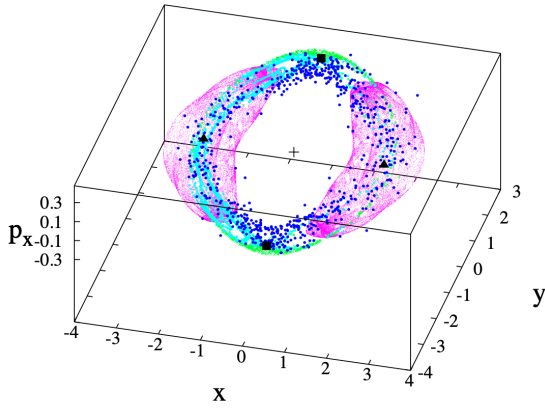


Figure 16. The 3D, (x, y, p_x) , projection of the unstable invariant manifolds of the simple unstable POs of uao and its symmetric family for $E_j = -0.165$, are plotted with green and cyan color respectively. The tori around the stable POs of sao and its symmetric family are drawn with magenta color. The blue points are the consequents of the toroidal zone of Fig. 14, as projected again in the 3D, (x, y, p_x) subspace of the space of section. The locations of the POs of the z-axis family, of the two uao’s and of the two sao’s are indicated with a cross, two black squares and two black triangles respectively.

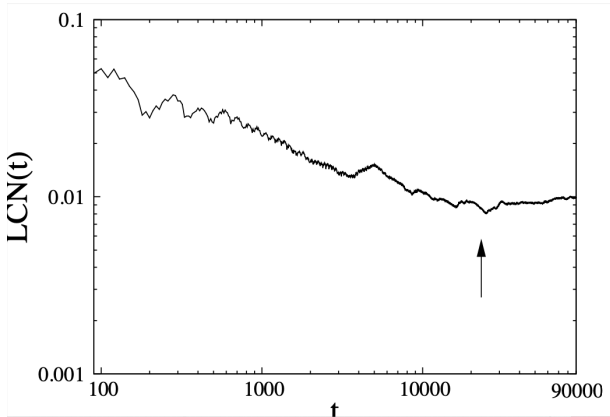


Figure 17. The variation of $LCN(t)$ (in log-scale) for the orbit in Fig. 15. The arrow indicates the time $t = 25000$ at which the points depart from the toroidal structure in Fig. 14.

Finally, the evolution of the diffusion volume for the orbit of the toroidal structure (Fig. 14) is depicted in Fig. 18d. The toroidal-structure-orbit is initially sticky to the unstable invariant manifolds of the two uao’s, which are guided through the invariant tori of either sao’s. As we see in Fig. 18d V_d increases with a decreasing rate up to the point that is indicated with an arrow, tending to level off. The indicated time corresponds again to the characteristic time at which the points of the toroidal structure leave the unstable manifolds, forming a cloud. We observe that, the diffusion volume increases, reaching a maximum value $V_d = 790$ at $T_d = 90000$, giving $u_d = 0.0088$. In the diagram of Fig. 18d we observe that the increasing rate is larger than this of the cloud in Fig. 18c. This is because the consequents are stuck initially in a smaller volume (the unstable invariant manifolds of the two uao’s, which are guided through the invariant tori of either sao’s) than the one occupied by the cloud in the previous case. When they expand outside this volume, they start to occupy larger volumes in phase space and the increasing diffusion rate is larger than this of the clouds. This is due to the fact that initially the volume of these consequents was smaller.

6 DISCUSSION AND CONCLUSIONS

The present study underlines the significance of the existing structure of the phase space in the neighborhood of POs for the determination of the orbital behaviour of orbits in the vicinity of the POs. Apart from the case, in which the perturbation of the initial conditions of a PO brings the perturbed orbits on nearby tori of other families, there are several kinds of stickiness, that may keep the orbit confined in the vicinity of a PO for times, dynamically significant in Galactic Dynamics. This may delay the diffusion of the orbit in remote phase space regions, in the same way that the trapping of a chaotic orbit in a restricted volume may even reinforce morphological features observed in disk galaxies (Patsis and Katsanikas 2014a; Patsis et al. 2022).

By perturbing the initial conditions of the vLPOs around the Lagrangian points $L_{1,2}$, we found five types of orbital behaviour:

(i) **Double-crescent, sticky chaotic structures:** The first type is represented by double-crescent structures with smooth color variation along their consequents in the 4D spaces of section. This means that they are at least close to a smooth surface in the 4D space. This morphology lasts for long integration times (of the order of a Hubble time). However, the points forming them are sticky

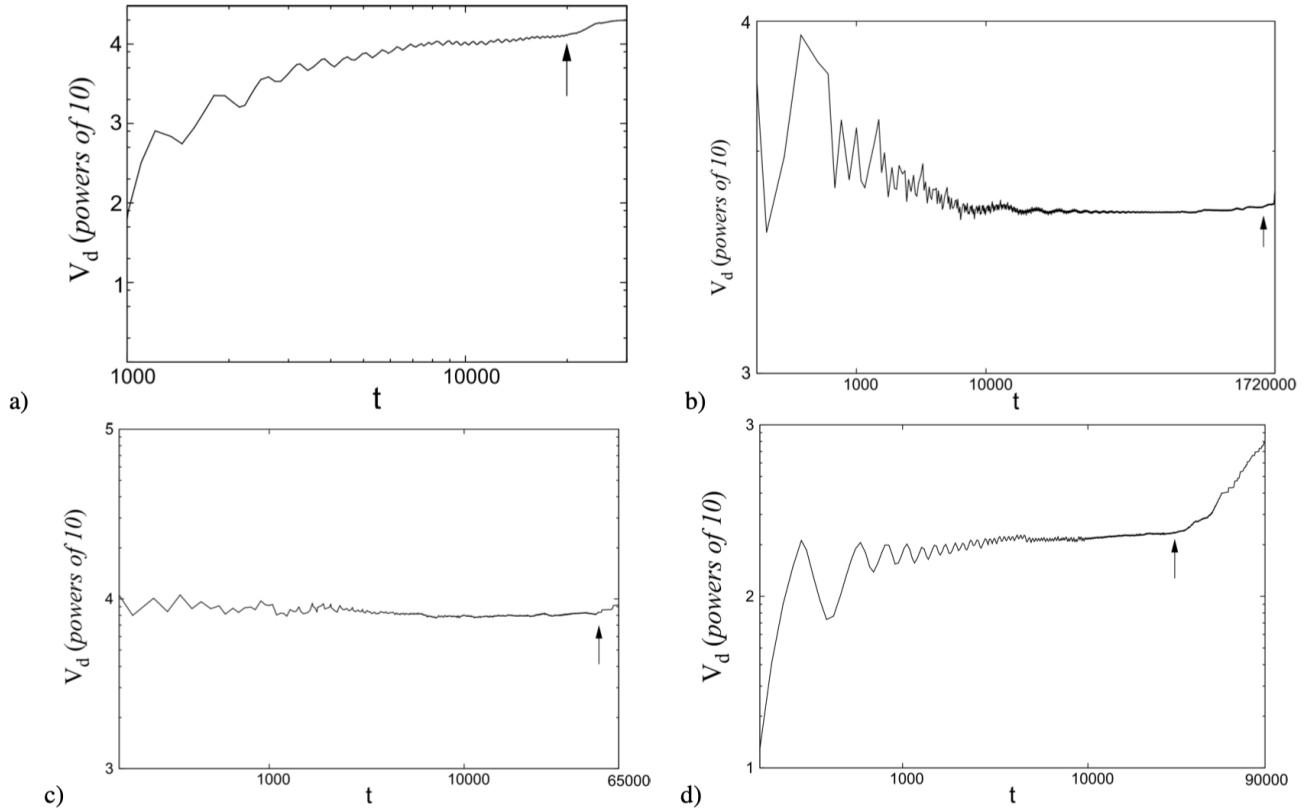


Figure 18. **a)** The time evolution of V_d (in log-scale) in the case of the double-crescent structure for $1000 \leq t \leq 30000$. **b)** The time evolution of V_d (in log-scale) at the case of the sticky torus for $10 \leq t \leq 1720000$. **c)** The time evolution of V_d (in log-scale) at the case of the cloud for $10 \leq t \leq 65000$. **d)** The time evolution of V_d (in log-scale) at the case of the toroidal zone for $10 \leq t \leq 90000$.

on the unstable invariant manifolds of the simple (or double) unstable POs around the Lagrangian points $L_{1,2}$. The manifolds are guided from the invariant tori that are found around the stable vertical periodic orbits associated with the Lagrangian points $L_{4,5}$. For larger integration times the points diffuse away of these structures and occupy larger volumes in the phase space. Thus, eventually, they are chaotic with large diffusion speeds.

(ii) **Clouds:** The second orbital type can be described as 4D clouds of points in the 4D spaces of section. The consequents have irregular distribution in the 3D projections and mixing of colors when colored according to their values in the fourth dimension. This is typical of a strong chaotic behavior, as also reflected in the large values of the Lyapunov characteristic numbers (LCN) of these orbits. Nevertheless, their expansion rate is decelerated, by the presence of the invariant tori around the sao POs. This keeps their u_d values relatively small.

(iii) **Quasi-periodic orbits on tori:** The third type are regular orbits forming tori with smooth color variation along their surfaces. In this case, their LCN tends to zero. These are quasi-periodic orbits around the stable vLPO4 and vLPO5 or around either branch of the sao's.

(iv) **Sticky tori:** The fourth type are the sticky tori. In the 4D spaces of section, these orbits stick on the tori around the stable vLPO4 and vLPO5 for long time. Eventually, these weakly chaotic orbits diffuse in phase space with small diffusion speeds.

(v) **Toroidal zones/structures:** Finally, we find the orbits we call toroidal zones or toroidal structures. These are orbits, sticky

on the unstable invariant manifolds of the two simple unstable uao POs, which are guided by the invariant tori around the sao's. Up to a certain time the consequents of these orbits stay on a quasi-regular toroidal-like zone retaining a smooth color variation along their surface. Then, this weakly chaotic behaviour turns to a strongly chaotic one, with totally irregular distribution of the consequents in the 3D projections, mixing of colors and large positive LCN . They are practically clouds of scattered points in the 4D spaces. Nevertheless, the diffusion of these orbits is small due to the presence of the the sao tori in the region.

Stickiness is ubiquitous in the neighborhood of the simple unstable vLPOs around $L_{1,2}$. Stickiness in chaos appears typically in orbits sticky to the asymptotic curves of the vLPO1,2 unstable invariant manifolds. They remain close to the tori of the vertical families of POs associated with $L_{4,5}$. Stickiness in chaos is also found in orbits remaining sticky to the asymptotic curves of the unstable invariant manifolds of the uao POs. In addition we also find sticky orbits to the sao, as well as to the vLPO4 and vLPO5, tori. In conclusion, the presence of the sao tori is very important for restricting the orbital diffusion from the region around the vLPOs.

A basic, general, conclusion of this study is that the presence of stickiness in the orbital behaviour of the orbits in our 3D Hamiltonian system, hinders the diffusion of chaotic orbits. We find that strongly chaotic orbits, with large LCN , have small diffusion speeds. Such orbits are the clouds and the orbits we called toroidal zones/structures. Contrarily, weakly chaotic orbits like those that

build the double crescent structures have large diffusion speeds. The difference between the two cases is the existence (former case) or the absence (latter case) of barriers, i.e. of nearby invariant tori, in the vicinity of the POs. Thus, although in the 6D phase space of a 3D system we can follow more paths, compared to a 2D system, for visiting all regions of a chaotic sea, in practice this is proven to be in many cases problematic. The complexity of the phase space plays a crucial role, since in the vicinity of the POs one can find several invariant structures (tori or manifolds) which in effect delay the diffusion of chaotic orbits.

The lack of observed structures away of the equatorial plane at the corotation region in galactic images indicates the absence of families that can act as obstacles for the diffusion of the orbits in the surrounding chaotic sea. This refers mainly to the sao and uao families which therefore are probably not populated in real galaxies.

Acknowledgements

We thank Prof. G. Contopoulos for fruitful discussions and very useful comments.

Data Availability

The data underlying this article will be shared on reasonable request to the corresponding author.

REFERENCES

- Agaoglou, M., Aguilar-Sanjuan, B., Garca-Garrido, V.J., Garca-Meseguer, R., Gonzalez-Montoya, F., Katsanikas, M., Krajčák, V., Naik, S., & Wiggins, S. (2019), "Chemical Reactions: A Journey into Phase Space" Zenodo. <https://doi.org/10.5281/zenodo.3568210>.
- Agaoglou, M., Aguilar-Sanjuan, B., Garca Garrido, V.J., Gonzalez-Montoya, F., Katsanikas, M., Krajčák, V., Naik, S., & Wiggins, S. (2020), "Lagrangian Descriptors: Discovery and Quantification of Phase Space Structure and Transport" Zenodo. <https://doi.org/10.5281/zenodo.3958985>.
- Agaoglou, M., Garca-Garrido, V. J., Katsanikas, M., & Wiggins, S. (2021), Communications in Nonlinear Science and Numerical Simulation, 103, 105993.
- Arnold, V.I., 1988, Geometrical Methods in the Theory of Ordinary Differential Equations, 2nd edition, Springer-Verlag NY.
- Arnold V.I., 1963, Russ. Math. Surveys 18, 9
- Aronica G., 2006, PhD Thesis, Ruhr-Universität Bochum
- Athanassoula E., Misiriotis A., 2002, MNRAS 330, 35
- Broucke R., 1969, "Periodic orbits in the elliptic restricted three-body problem", NASA Techn. Rep. 32, 1360
- Bountis T., Manos T., Antonopoulos C., 2012, Cel.Mech.Dyn.Ast. 113, 63
- Bureau M., Athanassoula E., 2005, ApJ 626, 159
- Bureau M., Aronica G., Athanassoula E., Dettmar R.-J., Bosma A., Freeman, K. C., 2006, MNRAS, 370, 753
- Carpintero DD, Muzzio JC. MNRAS 2020 Jun;495(2):1608-12.
- Cheung E., Athanassoula E., Masters K.L. et al. 2013, ApJ 779, 162
- Combes F., Debbasch F., Friedli D., Pfenniger D., 1990, A&A 233, 95
- Contopoulos G., 1981, A&A 102, 265
- Contopoulos G., 2004, "Order and Chaos in Dynamical Astronomy", Springer Verlag, Berlin-Heidelberg
- Contopoulos G., 1978, A&A, 64, 323.
- G. Contopoulos, P. Magnenat, and L. Martinet *Physica D* **6**, 123-136 (1982)
- G. Contopoulos, and B. Barbanis *Celest. Mech. Dyn. Astron.* **59**, 279-300 (1989)
- Contopoulos G., Barbanis B., 1985, A&A 153, 44
- Contopoulos G., Grosbøl P., 1989, A&AR, 1,261
- Contopoulos G., Harsoula M., Int.J.Bif.Ch 18,2929
- Contopoulos G., Harsoula M., 2010, Cel.Mech.Dyn.Ast. 107, 77
- Contopoulos G., Harsoula M., 2013, MNRAS 436, 1201
- Contopoulos G., Magnenat P., 1985, Celest. Mech. 37, 387
- Contopoulos G., Farantos S.C., Papadaki H., Polymilis C., 1994, Cel. Mech. 37, 387
- Erwin P., 2005, MNRAS 364,283
- C. Froeschlé *Astron. Astrophys.* **4**, 115-128 (1970)
- C. Froeschlé *Astron. Astrophys.* **16**, 172-189 (1972)
- Gardner E., Debattista V., Robin A., et al. 2014, MNRAS 438, 3275
- Geisel C.D., 2013, *Spacecraft Orbit Design in the Circular Restricted Three-Body Problem Using Higher-Dimensional Poincaré Maps*, PhD Thesis, Purdue University, West Lafayette, Indiana, USA
- Hadjidemetriou J., 1975, Celest. Mech. 12, 255
- Heggie D.C., 1985, Celest. Mech. 35, 357
- Heisler J., Merritt D., Schwarzschild M., 1982, Astroph.J 258, 490
- Hickson P., 1993, Astr. Lett. Comm. 29, 1
- Jorba A., Olle M., 2004, Nonlinearity 17, 691
- Katsanikas M., Patsis P.A., 2011, Int. J. Bif. Ch. 21-02, 467
- Katsanikas M., Patsis P.A., Contopoulos G., 2011a, Int. J. Bif. Ch. 21-08, 2321
- Katsanikas M., Patsis P.A., Pinotsis A.D., 2011b, Int. J. Bif. Ch. 21-08, 2331
- Katsanikas M., Patsis P.A., Contopoulos G., 2013, Int. J. Bif. Ch. 23-02, 1330005
- Kaufmann D. & Contopoulos G., 1996, A&A 309,381
- Kolmogorov, A.N., 1954, Dokl. Akad. Nauk USSR, 98, 527
- Kregel M., van der Kruit P.C., Freeman K.C., 2004, MNRAS 351, 1247
- Lange S., Richter M., Onken F. et al., 2014,haos 24, 024409.
- Li Z-Y., Shen J. 2012, ApJL 757L, L7
- Lukes-Gerakopoulos G., Katsanikas M., Patsis P.A. and Seyrich J. , 2016, Phys. Rev. D, 94, 024024
- Lütticke R., Dettmar R.-J., Pohlen M., 2000, A&A 362, 435
- Martinet L., Pfenniger D. 1987, A&A 173, 81
- Martinez-Valpuesta I., Shlosman I., Heller C., 2006, ApJ 637, 214
- Moser, J., 1962, Nachr. Akad. Wiss. Gött, II Math.- Phys Kl. 1-20
- Miyamoto M., Nagai R., 1975, PASJ, 27,533.
- Muzzio, Juan Carlos. " MNRAS, 2017471, no. 4 (2017): 4099-4110.
- Muzzio, Juan Carlos. " MNRAS, 473, no. 4 (2018): 4636-4643.
- Ollé M., Pacha J.R., Villanueva J., 2004, Cel. Mech. Dyn. Astr. 90, 89
- Ollé M., Pfenniger D., 1998, A&A, 334, 829
- Papadaki H., Contopoulos G., Polymilis C., 1995, in "From Newton to Chaos", Roy A.E., Steves B.A. (eds), pp 485-494, Plenum Press, New York
- Patsis P.A., 2005, MNRAS 358, 305
- Patsis P.A., Athanassoula E., 2019, MNRAS 490, 2740
- Patsis P.A., Grosbøl P., 1996, A&A 315, 371
- Patsis P.A., Manos T., Chavez-Velasquez L., Skokos Ch., Puerari, I. 2022, Physica D 42933050
- Patsis P.A. and Katsanikas M., 2014, MNRAS 445, 3525

- Patsis P.A. and Katsanikas M., 2014, 445, 3546
- Patsis P.A., Xilouris E., 2006, MNRAS 366, 1121
- Patsis P.A., Zachilas L., 1990, A&A 227, 37
- Patsis P.A., Zachilas L., 1994, Int. J. Bif. Ch. 4, 1399
- Patsis P.A., Skokos Ch., Athanassoula E., 2002, MNRAS 337, 578
- Pfenniger D., 1984, A&A 134, 373
- Pfenniger D., 1985a, A&A 150, 97
- Pfenniger D., 1985b, A&A 150, 112
- Plummer H.C., 1911, MNRAS 71, 460
- Poincaré H., 1892, “Les Méthodes Nouvelles de la Mécanique Céleste” Gauthier Villars, Paris I (1892), II (1893), III (1899); Dover (1957).
- Quillen A.C., Minchev I., Sharma S. et al., 2014, MNRAS 437, 1284
- Richter M., Lange S., Bäcker A., Ketzmerick R., 2014, PhRvE, 89,022902
- Romero-Gómez, M., Masdemont, J. J., Garcia-Gómez, C., & Athanassoula, E., 2009, Comm. Nonlinear Science Numerical Simulation, 14, 4123
- Romero-Gómez M., Athanassoula E., Masdemont J. J. & Garcia-Gómez C., 2007, A&A, 472, 63-75.
- Saha K., Gerhard O., 2013, MNRAS 430, 2039
- Saha K., Naab T., 2013, MNRAS 434, 1287
- Sánchez-Martin P., Romero-Gómez M., Masdemont J.J., 2016, A&A 588, A76
- Saito R.K., Zoccali M., Mc William A. et al., 2011, AJ 142, 76
- Sandage A., Bedke, J., 1994, The Carnegie Atlas of Galaxies. Volume II, Carnegie Inst. of Washington
- Skokos Ch., 2001, Physica D 159, 155
- Skokos Ch., 2010, Lect. Not. Phys., 790, 63
- Skokos Ch., Patsis P.A., Athanassoula E., 2002a, MNRAS 333, 847
- Skokos Ch., Patsis P.A., Athanassoula E., 2002b, MNRAS 333, 861
- Stöber J., Bäcker A., 2021, Phys. Rev. E, 103, 042208
- Tsoutsis P., Kalapotharakos C., Efthymiopoulos C., Contopoulos G., 2009, A&A 495, 743
- Vásquez S., Zoccali M., Hill V. et al. 2014, A&A 555, 91
- Vrahatis, M. N., Bountis, T. C., & Kollmann, M. , 1996, International Journal of Bifurcation and Chaos, 6(08), 1425-1437.
- Vrahatis M., Isliker H., Bountis T.C., 1997, Int. J. Bif. Ch. 7, 2707
- Wakamatsu K., Hamabe M., 1984, ApJS 56, 283
- Wegg C., Gerhard O., 2013, MNRAS 435, 1874
- Williams M. J, Zamojski M. A., Bureau M. et al., 2011, MNRAS 414, 2163
- Zachilas L., 1993, A&AS 97, 549
- Zachilas L., Katsanikas M., Patsis P. A. 2013, Int. J. Bif. Ch. 23, 1330023